

## ARTICLE

# 3D-printed microelectronics for integrated circuitry and passive wireless sensors

Sung-Yueh Wu<sup>1,2,3,\*</sup>, Chen Yang<sup>1,3,\*</sup>, Wensyang Hsu<sup>2</sup> and Liwei Lin<sup>1,3</sup>

Three-dimensional (3D) additive manufacturing techniques have been utilized to make 3D electrical components, such as resistors, capacitors, and inductors, as well as circuits and passive wireless sensors. Using the fused deposition modeling technology and a multiple-nozzle system with a printing resolution of 30 µm, 3D structures with both supporting and sacrificial structures are constructed. After removing the sacrificial materials, suspensions with silver particles are injected subsequently solidified to form metallic elements/interconnects. The prototype results show good characteristics of fabricated 3D microelectronics components, including an inductor–capacitor–resonant tank circuitry with a resonance frequency at 0.53 GHz. A 3D “smart cap” with an embedded inductor–capacitor tank as the wireless passive sensor was demonstrated to monitor the quality of liquid food (e.g., milk and juice) wirelessly. The result shows a 4.3% resonance frequency shift from milk stored in the room temperature environment for 36 h. This work establishes an innovative approach to construct arbitrary 3D systems with embedded electrical structures as integrated circuitry for various applications, including the demonstrated passive wireless sensors.

**Keywords:** additive manufacturing; radio-frequency passive sensors; 3D inductors and capacitors; three-dimensional printing; wireless sensing

*Microsystems & Nanoengineering* (2015) **1**, 2015013; doi:10.1038/micronano.2015.13; Published online: 20 July 2015

## INTRODUCTION

The three-dimensional (3D) additive printing process has attracted great interest in the field of rapid prototyping for a variety of applications due to its flexibility in geometrical designs and manufacturing<sup>1</sup> compared to subtractive manufacturing methods, such as mechanical machining and laser cutting<sup>2–4</sup>. In recent years, this technique has been applied to the field of microsystems due to improved capabilities in making structures with smaller feature sizes and better accuracies, including microfluidic systems<sup>5–11</sup>. Although arbitrary polymeric microfluidic systems can be readily constructed, the 3D printing process has not been widely applied to the general field of Microelectromechanical Systems (MEMS). One reason is the difficulty in producing good 3D conductive layers, which are essential in most functional devices, as special equipment and techniques are required<sup>3,4,12–15</sup>.

Here, we propose to use regular 3D printing equipment to construct 3D microstructures with embedded metallic elements by means of fillings of liquid metal paste to produce a variety of basic microelectronics components, such as resistors, capacitors, and inductors. This work is the first demonstration of the combined process of 3D additive polymer printing combined with liquid metal paste filling for use in potential practical applications. By connecting these basic components, one can build more complicated circuitries as well as numerous functional systems. As a proof-of-concept, we constructed a 3D radio-frequency (RF) passive circuit and further enhance the passive wireless sensing system for a practical demonstration—a polymeric “smart cap” with an embedded and wirelessly readable inductor–capacitor (LC)-resonant circuit, which could enable the rapid and built-in sensing for food safety detection in fluidic packages.

## DESIGN AND FABRICATION

Figure 1 illustrates the proposed 3D design and the fabrication steps. First, functional 3D structures are designed and constructed using the 3D printing technique. The hollow microchannels and cavities are designed in the 3D structures to be filled later with liquid metal paste. A hollow solenoid-shaped channel is formed as shown in Figure 1a1. To facilitate the liquid metal paste filling step, injecting holes are designed as the inlet/outlet ports for the solenoid channels, as shown in Figure 1a2. For direct frequency characterizations of the designed RLC circuitry, the solenoid-inductor structure has designated cavities as the ground-signal-ground (G-S-G) pads on the top surface for contact pads. After the 3D printing process, liquid metal paste is injected to form conductive electrical structures, as shown in Figure 1a3. The overflow of the liquid metal paste at the outlets on the top surface are flattened and used as the contact pads. The final solidification process cures the liquid metal paste to form solid structures, while the top surface of the device is planarized to remove the injecting holes.

Several basic microelectronic components were designed using the proposed approach, as shown in Figure 1b, including resistors, inductors, and capacitors. Specifically, the resistors are made of meander-shaped conductive wires embedded in the 3D structures, and the resistance of each wire is determined by the resistivity of the material of the wire as well as the cross-sectional area and the length of the wire. The inductors are designed to have the shape of a spiral coil, and the inductance can be estimated by the enclosed area of the coils and the number of turns of the coils. The capacitors are constructed in the form of two parallel-plates, and the capacitance is determined by the area

<sup>1</sup>Department of Mechanical Engineering, University of California, Berkeley, CA 94720, USA; <sup>2</sup>Department of Mechanical Engineering, National Chiao Tung University, Hsinchu 30010 and <sup>3</sup>Berkeley Sensor and Actuator Center (BSAC), University of California, Berkeley, CA 94720, USA

\*Both Sung-Yueh Wu and Chen Yang contributed equally to this work.

Correspondence: Liwei Lin (lwlw@me.berkeley.edu)

Received: 21 April 2015; revised: 9 June 2015; accepted: 9 June 2015

of the plate, the permittivity of the polymeric material and the distance between the two plates. Functional electrical circuits can be made by further integration, e.g., connecting a solenoid inductor and a parallel-plate capacitor to form a LC-resonant tank, as shown in Figure 1c. Due to the geometric flexibility of the

3D printing, the 3D metal-embedded micro-systems provide great flexibility for possible practical applications. For example, the design of a “smart cap” is proposed as shown in Figure 1d for use in liquid food package applications. The cap has an embedded LC-resonant circuit to detect the quality of the liquid

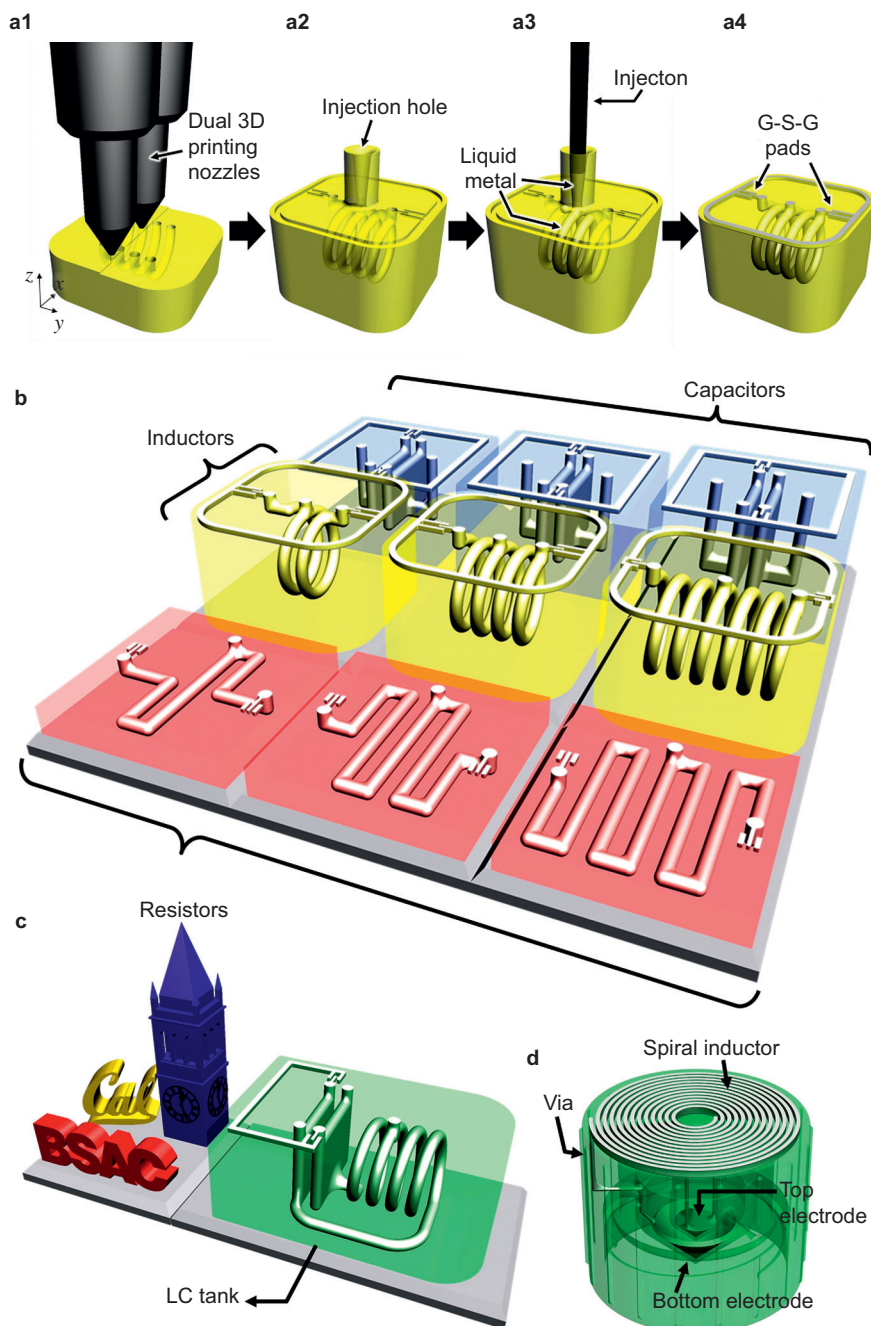


**Figure 1** Schematic diagram of the additive 3D manufacturing process including the filling of liquid metal paste for producing basic microelectronic components, integrated circuitries, and a passive wireless sensor. (a) The 3D fabrication process with embedded and electrically conductive structures. (b) 3D microelectronics components, including parallel-plate capacitors, solenoid-type inductors, and meandering-shape resistors. (c) A 3D LC tank, which is formed by combining a solenoid-type inductor and a parallel-plate capacitor. (d) A wireless passive sensor demonstration of a “smart cap,” containing the 3D-printed LC-resonant circuit. The degradation of the liquid food inside the liquid package can cause the changes of the dielectric constant and the shift of the resonance frequency of the LC circuitry. A wireless inductive reader is used to monitor the signals in real time.

food inside the package. The sensing principle is based on the capacitance changes of the liquid food due to its deterioration over time. This information is monitored wirelessly in real time by observing the resonance frequency shifts of the LC tank via an inductive reader. As such, this smart cap could enable a passive, wireless sensing scheme without the need to open the packages for food safety inspection.

The prototype fabrication process uses the 3D printing machine, ProJet HD 3000, based on the fused deposition modeling technology<sup>16</sup> with a printing resolution of 30  $\mu\text{m}$ . During the printing process, polymer materials are heated and ejected from the nozzles of the inkjet printer. Building (VisiJet EX 200, 3D Systems Inc., Rock Hill, SC, USA)<sup>17</sup> and sacrificial materials (VisiJet S100, 3D Systems Inc., Rock Hill, SC, USA)<sup>18</sup> are deposited alternatively from the dual nozzles to form the printed samples, in which the building material defines the molding structure, while the sacrificial material occupies the hollow channels<sup>19</sup>. Afterwards, a post-printing process is conducted to remove the sacrificial materials. First, the whole 3D-printed sample is immersed in a mineral oil bath at 80 °C to dissolve the sacrificial material. Second, the residual mineral oil is removed by thoroughly washing with detergent and water in sequence. The liquid metal paste comprised of a silver suspension (Pelco 16040-30, Ted Pella Inc., Redding, CA, USA)<sup>20</sup> is then injected into the channels and cavities. Next, the as-filled sample is kept at room temperature for 2 h for the solidification process. The detailed fabrication method flow can be found in the Supplementary Information. These components can be scaled up or down based on the capabilities of the specific type of 3D printer. However, the liquid metal paste filling process has practical limits. Specifically,

smaller channels (diameter of 400  $\mu\text{m}$  or smaller in our experiments) have large flow resistance that prevents the filling process, and the 600- $\mu\text{m}$  diameter design is the optimal channel size in this work using the ProJet HD 3000 printer, Hewlett-Packard Company, Palo Alto, CA, USA.

## RESULTS

The prototype 3D-printed microelectronics components without the liquid metal paste are fabricated as shown in the optical photo of Figure 2a, with a one-cent US coin shown for reference. After removing the sacrificial materials and injecting the liquid metal paste, the resulting functional components and the LC circuitry are shown in Figure 2b. Note that the volume of the silver suspension shrank after the solidification process, which could leave voids inside the metal traces. By repeating the filling operations, these voids are minimized, thereby improving the electrical conductivity. With five times repeated filling, the measured average volume-filling ratio reaches 68.7%, as characterized in the cross-section views of these components shown in Figure 2c. The electrical performances of the fabricated passive components were characterized as follows. The DC I-V curves of the resistors are measured using a semiconductor parameter analyzer (HP 4145B, Hewlett-Packard Company, Palo Alto, CA, USA). The two-port RF S-parameter spectra of the inductors, capacitors, and LC tank are measured using Cascade Microtech ACP40-GSG-200, Cascade Microtech Inc., Beaverton, OR, USA, probes and a network analyzer (Agilent E5071B, Agilent Technologies, Santa Clara, CA, USA). The parasitic effects of G-S-G pads are de-embedded accordingly.

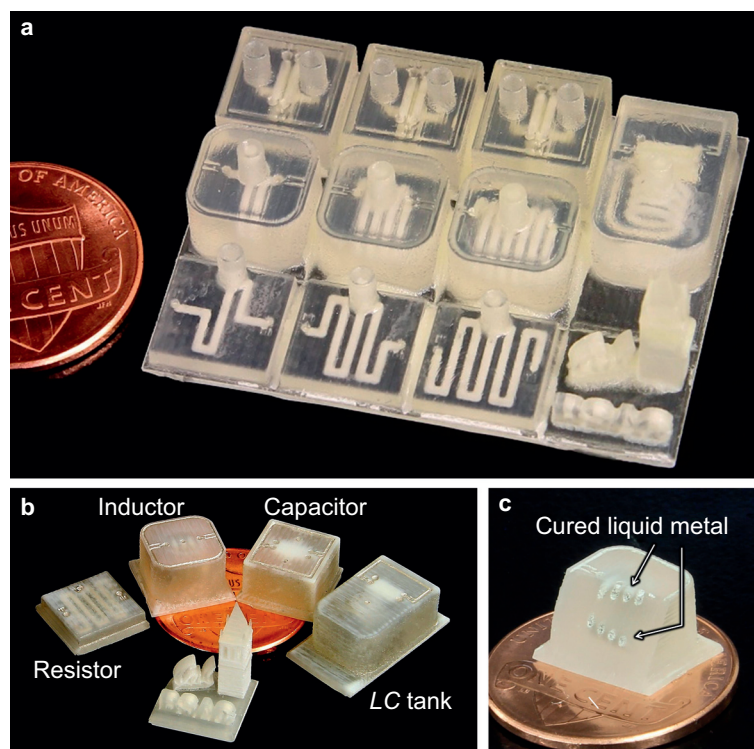
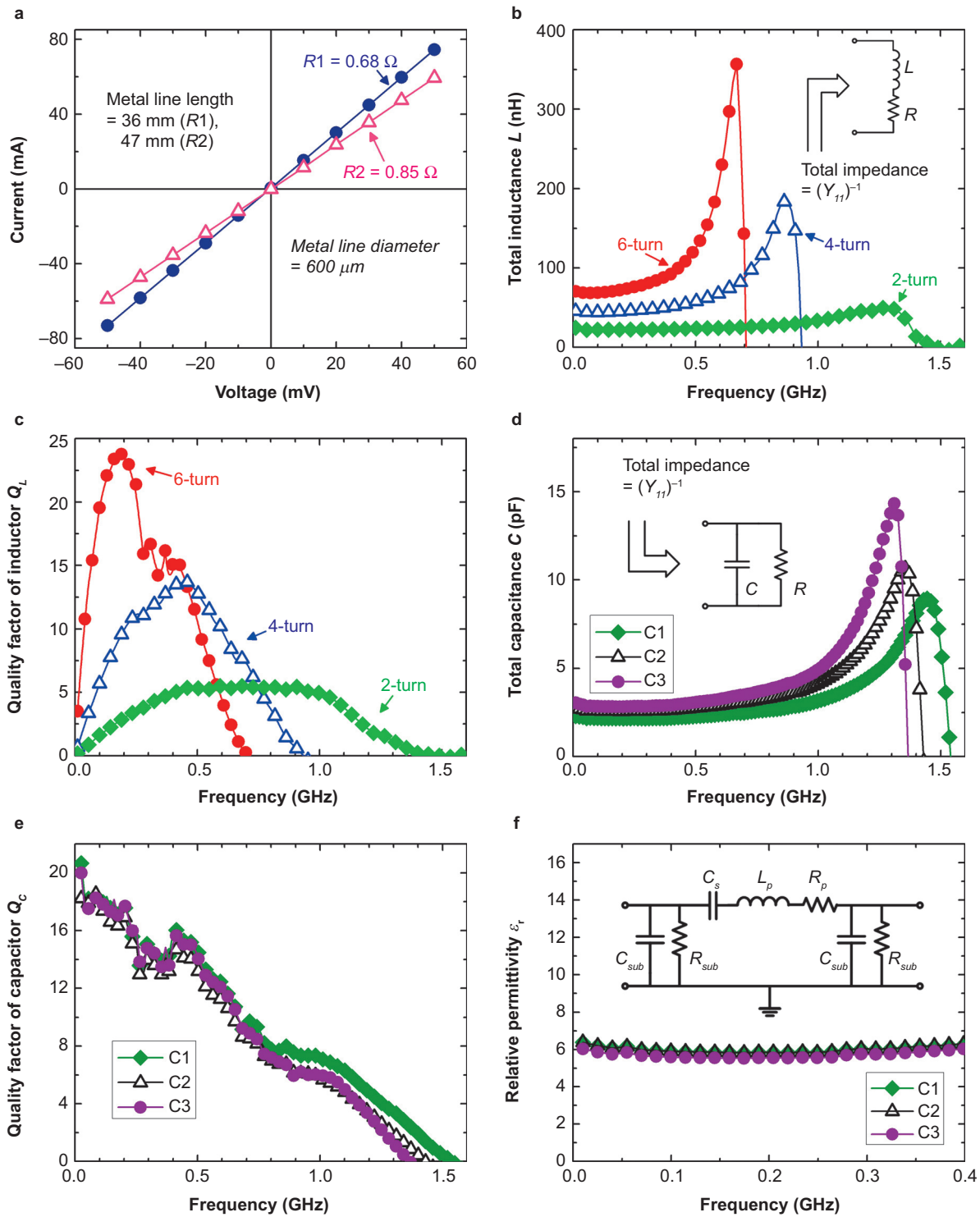


**Figure 2** (a) An optical image showing fabricated microelectronics components produced using the 3D printing process without the embedded conductive structure compared with a one-cent US coin. (b) Fabricated 3D components, including resistors, inductors, and capacitors, and an LC tank after the liquid metal paste filling and curing process. (c) The cross-sectional view of a 4-turn solenoid coil. The overall size of the prototype resistor, inductor, and capacitor are 10 × 10 × 2.4, 10 × 10 × 6.4, and 10 × 10 × 6.4 mm<sup>3</sup>, respectively, whereas the size of the LC tank is 10 × 20 × 6.4 mm<sup>3</sup>.

**Resistors**

The DC  $I$ - $V$  curves of two resistors with different designs are shown in Figure 3a. The equivalent conductivity  $\sigma$  of the filled metal is calculated as:

$$\sigma = \frac{I}{R \cdot S} \quad (1)$$



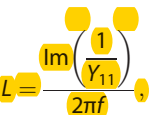
where  $R$  is the total resistance,  $I$  is the length of the conductor, and  $S$  is the cross-sectional area of the conductor structure based on the real volume-filling ratio. The cross-sectional shape of the metal traces is circular, with a diameter of 600  $\mu\text{m}$ , and length is 36 mm and 47 mm for resistor  $R_1$  and  $R_2$ , respectively. The overall resistances of  $R_1$  and  $R_2$  are measured as 0.68  $\Omega$  and 0.85  $\Omega$ ,

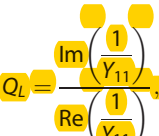
**Figure 3** Measurement results of 3D microelectronic components and an LC tank. (a) DC  $I$ - $V$  curves of 3D-printed resistors. (b) Total inductance  $L$  and (c) quality factor  $Q_L$  of 3D-printed RF inductors with different numbers of turns. (d) Total capacitance  $C$ , (e) quality factor  $Q_C$  and (f) calculated relative permittivity  $\epsilon_r$  of 3D-printed RF capacitors with different overlapping areas.

respectively. The average  $\sigma$  is found to be as high as  $2.8 \times 10^5 \text{ S}\cdot\text{m}^{-1}$ , which is approximately 10.5% of the value for ideal silver paste<sup>19</sup>. The difference comes from the poor packing density of the silver particles inside the channel after the solidification process (Supplementary Figure S1).

## Inductors

The measured two-port  $S$ -parameters of the fabricated inductors are converted to  $Y$ -parameters, and then the inductor performances are extracted as<sup>21</sup>:

$$L = \frac{\text{Im} \left( \frac{1}{Y_{11}} \right)}{2\pi f}, \quad (2)$$


$$Q_L = \frac{\text{Im} \left( \frac{1}{Y_{11}} \right)}{\text{Re} \left( \frac{1}{Y_{11}} \right)}, \quad (3)$$


where  $L$  is the total inductance,  $Q_L$  is the quality factor of the inductor, and  $f$  is the frequency.

Figure 3b and 3c show the measured inductance and quality factor of the inductors with different numbers of coil turns,  $N$ . These solenoid-shaped inductors have a designed diameter of 4 mm. The cross-sectional shape of the metal traces is circular with a diameter of 600  $\mu\text{m}$ . The line spacing between adjacent windings is 400  $\mu\text{m}$ . In Figure 3b, the measured total inductance  $L$  increases as  $N$  increases. For example, the inductances at 0.4 GHz are 23 nH, 51 nH, and 92 nH for inductors with 2, 4, and 6 turns, respectively. For each inductor, the  $L$  increases first as the frequency increases and then reaches a maximum value due to self-resonance. For example, the inductance of the 6-turn inductor increases from 92 nH at 0.4 GHz to over 350 nH approximately 0.67 GHz. For frequencies above the resonance, the inductance rapidly decreases. The frequency at which the  $L$  drops to zero, i.e., the self-resonance frequency  $f_0$  is 1.49 GHz, 0.93 GHz, and 0.71 GHz for the inductors with 2, 4, and 6 turns, respectively. Note that larger  $N$  corresponds to smaller  $f_0$  due to the larger inductance. Figure 3c shows the measured quality factors. The quality factor first increases as the frequency increases and then decreases to zero due to the high loss at the self-resonance frequency. Note that higher inductance leads to higher quality factor, which proves that 3D inductors are helpful in reducing the energy losses. For example, the 6-turn inductor has the highest  $Q_L$  of approximately 24 at 0.19 GHz, whereas the 2-turn inductor shows a maximum  $Q_L$  of 5.6 at 0.70 GHz. During the magnetic energy storage cycles in the inductors, the energy loss mechanisms mainly include the skin-effect induced ohmic losses in the conductor and the electric field energy losses due to parasitic capacitance.

## Capacitors

The measured  $S$ -parameters of the capacitors are converted to  $Y$ -parameters, and then the capacitor performances are extracted as<sup>22</sup>:

$$C = \frac{\text{Im}(Y_{11})}{2\pi f}, \quad (4)$$

$$Q_C = \frac{\text{Im}(Y_{11})}{\text{Re}(Y_{11})}, \quad (5)$$

where  $C$  is the total capacitance,  $Q_C$  is the quality factor of the capacitor, and  $f$  is the frequency.

The measured total capacitances and quality factors of three parallel-plate capacitors are shown in Figure 3d and e, respectively. The rectangular-shaped parallel-plate type capacitors ( $C_1$ ,  $C_2$ , and  $C_3$ ) have different overlapping areas (11.4, 14.08, and 16.72  $\text{mm}^2$ , respectively) with the same gap of 400  $\mu\text{m}$ . For each capacitor, the capacitance  $C$  initially increases as the frequency increases and reaches up to maximum to form the self-resonance ( $>1 \text{ GHz}$ ) due to the parasitic inductance. For example, the capacitance of capacitor  $C_3$  increases from 3 pF at 0.1 GHz to over 14.3 pF at approximately 1.31 GHz. After the peak, the capacitance rapidly decreases. The frequency at which the  $C$  decreases to zero, i.e., the self-resonance frequency  $f_0$  is 1.53 GHz, 1.43 GHz, and 1.36 GHz for  $C_1$ ,  $C_2$ , and  $C_3$ , respectively. Note that a larger overlapping area corresponds to a smaller  $f_0$  due to the higher capacitance. The extracted quality factors  $Q_C$  of three capacitors at low frequency are approximately 18–20, which are values comparable with those of general metal-insulator-metal (MIM) capacitors<sup>22</sup>; these quality factors can be further increased by decreasing the electrode gap  $d$ . As the frequency increases, the quality factors of three capacitors reduce gradually and then reach zero at approximately 1.4 GHz.

Because the building material (VisiJet EX 200)<sup>17</sup> serves as the dielectric material for the capacitors, its dielectric constant ( $\epsilon_r$ ) determines the performance of the capacitors; however, there are no prior reported data on the dielectric constant of VisiJet EX 200. To study  $\epsilon_r$ , a conventional  $\Pi$ -type lumped element equivalent circuit<sup>23</sup> is designed, as shown in the inset of Figure 3f. The impedance of the parallel-plates is modeled as the serial combination of a capacitor ( $C_s$ ), a parasitic inductor ( $L_p$ ) and a parasitic resistor ( $R_p$ ). The substrate parasitic effects are modeled as  $C_{\text{sub}}$  and  $R_{\text{sub}}$  at each symmetric port, which represent the effective capacitance and resistance, respectively, between the signal port and ground. In the series branch of parallel-plates,  $C_s$  will be the dominant element of the branch impedance ( $1/Y_{12}$ ) in the lower frequency range, which is far below the self-resonance frequency. Thus, the value of  $C_s$  could be extracted as:

$$C_s = \frac{\text{Im}(-Y_{12})}{2\pi f}. \quad (6)$$

Next, the dielectric constant of building material is calculated as:

$$\epsilon_r = \frac{C_s d}{\epsilon_0 A}, \quad (7)$$

where  $A$  is the overlapping area and  $d$  is the gap. The extracted relative dielectric constant  $\epsilon_r$  values from all the three devices are shown in Figure 3f, which are approximately 6, with very good consistency.

## Improved inductors and an LC tank

Magnetic materials can be easily integrated into the prototype 3D solenoid inductors by designing openings inside the coils to allow for the placements of magnetic materials to enhance the inductance. For example, one can insert a magnetic bar (Fair-Rite® 3061990861, Fair-Rite Products Corp., Wallkill, NY, USA)<sup>24</sup> into a 3D solenoid inductor manually. Figure 4a shows the preliminary results on the prototype 3D-printed inductors with inserted magnetic bars. The inductance is found to increase due to the addition of the magnetic core, and larger number of coil turns is found to lead to higher increases of the inductance. Specifically, the 6-turn coil device exhibits inductance enhancements over the reference air-core inductor are in the range of

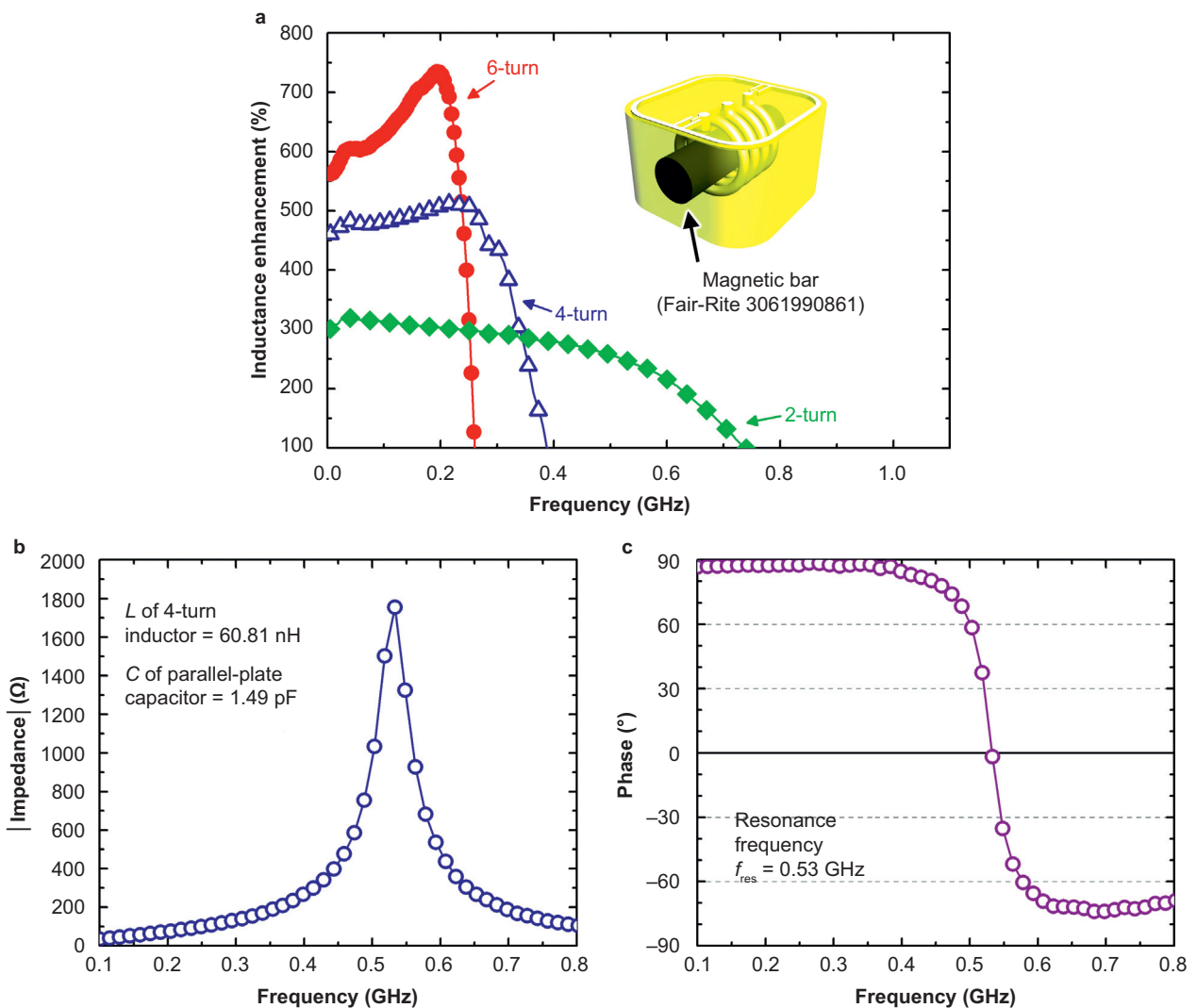


**Figure 4** (a) Measured inductance enhancements of 3D solenoid inductors with magnetic cores compared to the reference air-core inductors. (b) Impedance magnitude vs. frequency and (c) phase vs. frequency of a 3D-printed RF LC-resonant circuit with the inductor and capacitor connected in parallel.

approximately 550% to 734% over the frequency range of 0.01 GHz to 0.2 GHz.

Based on the same fabrication process, prototype LC tank circuits were constructed. The resonance frequency  $f_{\text{res}}$  of LC tank is derived as:

$$f_{\text{res}} = \frac{1}{2\pi\sqrt{LC}} \quad (8)$$

The measured frequency responses of the prototype device consisting of a 4-turn solenoid and a parallel-plate capacitor are shown in Figure 4b and c. In this case, the cross-sectional shape of the metal traces is circular, with a diameter of 600 μm, and the line spacing between the adjacent winding wires of the solenoid is 400 μm. The rectangular-shaped parallel-plate capacitor has an area of 8.36 mm<sup>2</sup>, with a gap of 400 μm. As the frequency increases, the magnitude of the impedance increases and reaches its maximum at 1.75 kΩ at the resonant frequency of 0.53 GHz, as shown in Figure 4b. The bandwidth is extracted as 40.72 MHz, based on  $1/\sqrt{2}$  of the peak impedance value. The calculated

quality factor  $Q$  is 13, which could be further increased by improving the material conductivity. Figure 4c shows the phase versus frequency plot.

#### BUILT-IN LC-RESONANT SENSOR

The 3D-printed LC tanks are further demonstrated as passive, wireless-resonant sensors that can be used in applications in food quality monitoring. Specifically, the LC sensor features passive operation without power consumption and wireless reading capability.<sup>25–32</sup> In the prototype demonstration, the LC sensor is embedded in the design of a “smart cap,” which has the required 3D geometry similar to a typical cap used in liquid food packages. The whole structure is fabricated using the 3D additive manufacturing process.

#### Design

Figure 5a illustrates the sensing architecture of the proposed cap with the embedded LC tank sensor. In this design, the circuit is composed of an inverted-cone-shape capacitor and a planar spiral-shaped inductor to form the LC-resonant circuit. By flipping

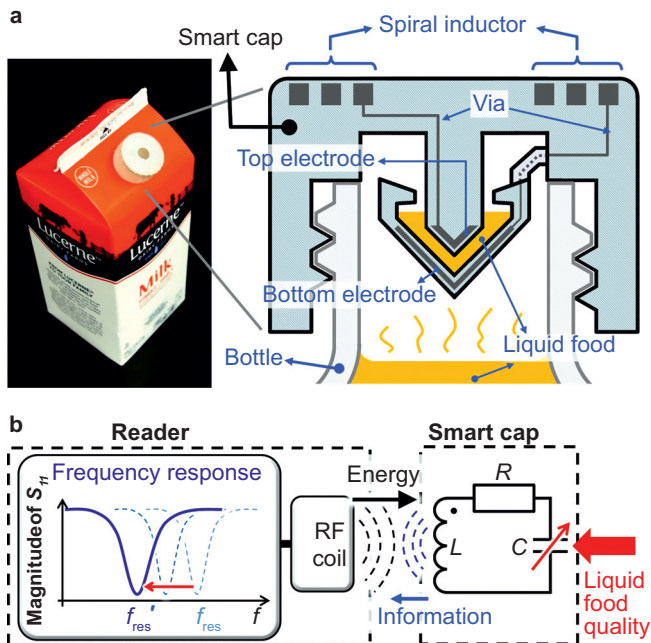


**Figure 5** The proposed “smart cap” for rapid detection of liquid food quality featuring wireless readout: (a) the smart cap with a half-gallon milk package, and the cross-sectional schematic diagram; (b) sensing principle with the equivalent circuit diagram.

the food package upside down, the liquid food is trapped inside the capacitor gap of the LC tank and acts as the dielectric material. The LC tank’s  $f_{\text{res}}$  is determined by the dielectric constant of the liquid food. When the liquid deteriorates, the value of  $f_{\text{res}}$  can shift as a result of the change of dielectric constant. The value of  $f_{\text{res}}$  can be detected wirelessly using an RF reader, as shown in Figure 5b. By imposing a frequency-swept electrical field in the reader coil, the LC tank stores energy due to near-field inductive coupling and exhibits electrical oscillation. The most pronounced oscillation occurs when the driving frequency matches the LC tank’s resonance frequency because, at this point, the LC tank absorbs the most electromagnetic energy. This resonance induces a negative peak in reader coil’s reflection coefficient  $|S_{11}|$  spectrum, as measured by a network analyzer<sup>33</sup>. By recording this peak,  $f_{\text{res}}$  is tracked wirelessly, and the quality of the liquid food is detected in real time without the need to open the package.

## Test results and discussion

Figure 6a-d show the fabricated cap structures, which are compatible with a half-gallon milk package. The outer diameter of the cap is 32 mm. The pitch and number of turns of the spiral inductor are 980  $\mu\text{m}$  and 12.5, respectively. The via-channel diameter is 600  $\mu\text{m}$ . Other detailed dimensions are shown in Supplementary Figure S2. Caps with the inverted-cone-shape capacitor gap as well as flat gap designs are fabricated and tested. The inverted-cone-shape design is used to eliminate air bubbles during the operations because liquid food can be trapped in the cavity by flipping the package while the air bubbles escape from the cavity to the top due to their own buoyant force (Supplementary Figure S3).

For wirelessly measuring the electrical resonance frequency of the smart cap, an RF reader coil with outer diameter of 30 mm and 13 turns was designed and constructed by manually winding an enameled insulated wire (diameter 1.15 mm). The reader coil

was connected to the network analyzer and inductively coupled to the cap, with a distance of 3 mm. The  $S_{11}$  spectrum of reader coil was measured, from which the  $f_{\text{res}}$  of the cap was tracked and characterized. Experimentally, fresh milk was stored under the room temperature (22 °C) environment to accelerate the degradation process, and the value of  $f_{\text{res}}$  of the LC tank was recorded after 0, 12, 24, and 36 h, as shown in Figure 6e. The value of  $f_{\text{res}}$  is observed to gradually decrease, indicating the increase of the dielectric constant of the degrading milk. Figure 6f shows the results from the milk samples at 22 °C and 4 °C versus time, with average measurement error of  $\pm 0.10$  MHz (three different tests). Under the storage condition at 4 °C, the value of  $f_{\text{res}}$  was found to remain at approximately 51.65 MHz, with a small shift of 0.12% after 36 h. In contrast, under the storage condition at 22 °C,  $f_{\text{res}}$  decreased by 4.3% after 36 h. As such, the frequency shifts as a result of the capacitance changes were validated here via wireless sensing. The corresponding dielectric constant changes can be extracted from these data as 9.2% under the storage condition at 22 °C, with a corresponding resolution of  $\pm 0.19\%$  in frequency, corresponding to  $\pm 0.39\%$  in dielectric constant in this prototype demonstration. Previously, various impedance devices have been used by the food and manufacturing industries and public health agencies to estimate the product shelf-life and the level of microbial contaminations<sup>27,34,35</sup>. However, these measurements are often converted to “bacterial counts” to satisfy a specific FDA ordinance (see the example for milk<sup>36</sup>) with further characterizations. Nevertheless, these prior reports have shown that changes in the ionic composition of a culture medium can either increase or decrease its electrical conductivity and capacitance by factors such as temperature, microbial cell density, microbial growth, and medium conductivity. The advantage of the demonstrated smart cap here is to reduce the possibility of contamination and provide the capability of wireless remote sensing.

With the flexibility of the geometry design of 3D printing and the demonstrated metallization method, other meaningful designs are expected to be produced. For example, *in-vivo* implants could further evolve to “smart implants” (e.g., smart spinal implants) with embedded transducer circuits to wirelessly transmit the local information, such as pressures and drug concentrations.

## CONCLUSION

Design, fabrication, and characterization processes for 3D-printed microelectronics components and circuitry by the combination of 3D printing and liquid metal paste filling techniques were developed. These components include various resistors, inductors, and capacitors, and circuits include LC-resonant tanks. The preliminary results demonstrate the good consistency of these 3D-printed devices with the analytical expectations and indicate the possible performance enhancements and system integration based on the 3D structures. As a demonstration example, a 3D “smart cap” with embedded LC tank as the passive wireless sensor was constructed for the application of monitoring the quality of liquid food (e.g., milk and juice). In this application, as the liquid food deteriorates, the dielectric constant of the liquid changes and the shift in the resonance frequency of the embedded 3D LC tank can be detected wirelessly by an inductively coupled reader in real time. The results showed a 4.3% frequency shift for a milk package stored under the room temperature environment for 36 h. The positive results indicate that 3D devices with embedded metallic components can open up a new class of applications in devices (beyond the passive wireless sensors) that benefit from 3D structures with embedded metallic conductors.

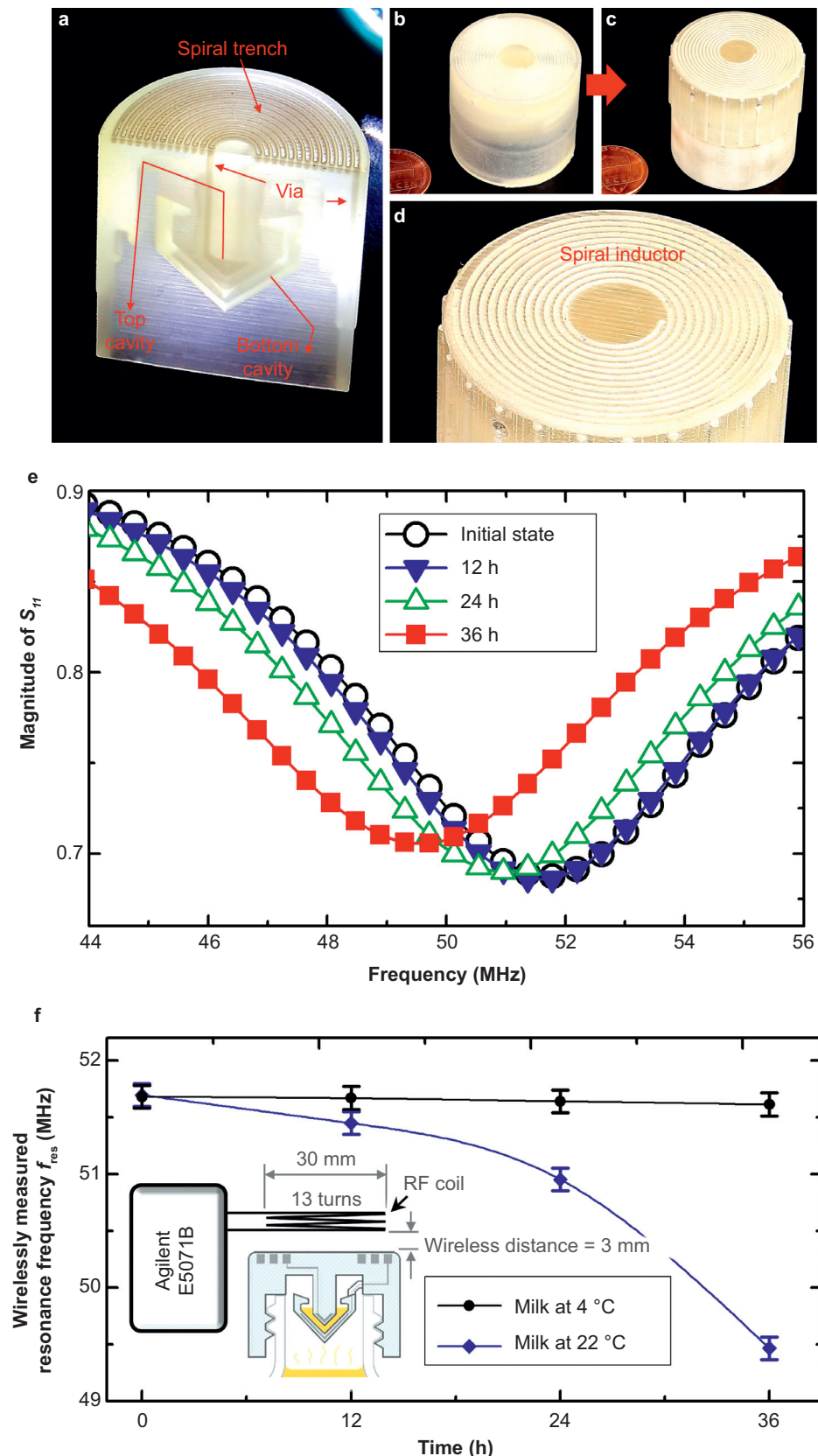


**Figure 6** Fabricated devices. (a) Cross-sectional view of a fabricated smart cap; (b) optical image of a completed 3D cap structure with a one-cent coin; (c) the fabricated cap after the liquid metal filling process; and (d) magnified optical image showing the spiral inductor around the top surface of the cap. Test results of wireless LC tank sensors from the RF reader: (e) magnitude versus frequency curves with milk at 22 °C after 0, 12, 24, and 36 h; (f) resonance frequency versus time for a milk sample at 4 °C and a milk sample at 22 °C.

## ACKNOWLEDGEMENTS

Mr. Sung-Yueh Wu is supported by the "Ministry of Science and Technology of Taiwan" (Grant No. 103-2917-I-009-192). The authors also thank Prof. Albert P. Pisano for his help with the measurement equipment.

## COMPETING INTERESTS

The authors declare no competing financial interest.

## REFERENCES

- 1 Lipson H, Kurman M. *Fabricated: The New World of 3D Printing*. John Wiley & Sons, Hoboken, NJ, USA, 2013.
- 2 Walker JR, Dixon B. *Machining Fundamentals Ninth Edition*. The Goodheart-Willcox Company, Inc. Tinley Park, IL, USA, 2014.
- 3 Dubey AK, Yadava V. Laser beam machining—a review. *International Journal of Machine Tools & Manufacture* 2008; **48**: 609–628.
- 4 Mahdavifar A, Xu J, Hovaizi M et al. A nitrocellulose-based microfluidic device for generation of concentration gradients and study of bacterial chemotaxis. *Journal of the Electrochemical Society* 2014; **161**: B3064–B3070.
- 5 Therriault D, White SR, Lewis JA. Chaotic mixing in three-dimensional micro-vascular networks fabricated by direct-write assembly. *Nature Materials* 2003; **2**: 265–271.
- 6 Kitson PJ, Rosnes MH, Sans V et al. Configurable 3D-printed millifluidic and microfluidic 'lab on a chip' reactionware devices. *Lab on a Chip* 2012; **12**: 3267–3271.
- 7 Paydar OH, Paredes CN, Hwang Y et al. Characterization of 3D-printed microfluidic chip interconnects with integrated o-ring. *Sensors and Actuators A: Physical* 2014; **205**: 199–203.
- 8 Comina G, Suska A, Filippini D. PDMS lab-on-a-chip fabrication using 3D printed templates. *Lab on a Chip* 2014; **14**: 424–430.
- 9 Gross BC, Erkal JL, Lockwood SY et al. Evaluation of 3D printing and its potential impact on biotechnology and the chemical sciences. *Analytical Chemistry* 2014; **86**: 3240–3253.
- 10 Erkal JL, Selimovic A, Gross BC et al. 3D printed microfluidic devices with integrated versatile and reusable electrodes. *Lab on a Chip* 2014; **14**: 2023–2032.
- 11 Lee KG, Park KJ, Seok S et al. 3D printed modules for integrated microfluidic devices. *RSC Advances* 2014; **4**: 32876–32880.
- 12 Hu J, Yu M-F. Meniscus-confined three-dimensional electrodeposition for direct writing of wire bonds. *Science* 2010; **329**: 313–316.
- 13 Adams JJ, Duoss EB, Malkowski TF et al. Conformal printing of electrically small antennas on three-dimensional surfaces. *Advanced Materials* 2011; **23**: 1335–1340.
- 14 Ladd C, So J-H, Muth J et al. 3D printing of free standing liquid metal microstructures. *Advanced Materials* 2013; **25**: 5081–5085.
- 15 Ahn BY, Duoss EB, Motala MJ et al. Omnidirectional printing of flexible, stretchable, and spanning silver microelectrodes. *Science* 2009; **323**: 1590–1593.
- 16 3D Systems. ProJet™ HD 3000 Technical Specifications. 3D Systems Inc., Rock Hill, SC, USA, 2009; <http://www.3dcreationlab.co.uk/pdfs/projet-hd-3000.pdf>.
- 17 3D Systems. Material Safety Data Sheet – EX 200. 3D Systems Inc., Rock Hill, SC, USA, 2012; <http://www.3dsystems.com/products/datafiles/visijet/msds/visijet-crystal/24184-S02-00-B-MSDS-US-English-EX-200-Crystal.pdf>.
- 18 3D Systems. Material Safety Data Sheet – SR 100. 3D Systems Inc., Rock Hill, SC, USA, 2012; <http://www.3dsystems.com/products/datafiles/visijet/msds/s100-s300/23126-S02-02-B-MSDS-US-Visijet-S100-S300.pdf>.
- 19 Yang C, Wu S-Y, Glick C et al. 3D printed RF passive components by liquid metal filling. The 28th IEEE International Conference on Micro Electro Mechanical Systems (IEEE MEMS 2015); 18–22 Jan 2015; Estoril, Portugal; 2015: 261–264.
- 20 Ted Pella. Technical Notes. Ted Pella Inc., Redding, CA, USA, 2005; [http://www.tedpella.com/technote\\_html/16040-30%20TN.pdf](http://www.tedpella.com/technote_html/16040-30%20TN.pdf).
- 21 Yang C, Liu F, Ren TL et al. Ferrite-integrated on-chip inductors for RF ICs. *IEEE Electron Device Letters* 2007; **28**: 652–655.
- 22 Parthasarathy S, Swaminathan B, Sundaram A et al. Design considerations for BEOL MIM capacitor modeling in RF CMOS processes. 23rd International Conference on VLSI Design; 3–7 Jan 2010; Bangalore, India; 2010: 188–193.
- 23 Vogel RW. Analysis and design of lumped- and lumped-distributed-element directional couplers for MIC and MMIC applications. *IEEE Transactions on Microwave Theory and Techniques* 1992; **40**: 253–262.
- 24 Fair-Rite®. Part Datasheet 3061990861. Fair-Rite Products Corp., Wallkill, NY, USA, 2013; [http://www.fair-rite.com/catalog\\_pdfs/3061990861.pdf](http://www.fair-rite.com/catalog_pdfs/3061990861.pdf).
- 25 Ong KG, Grimes CA, Robbins CL et al. Design and application of a wireless, passive, resonant-circuit environmental monitoring sensor. *Sensors and Actuators A: Physical* 2001; **93**: 33–43.
- 26 Akar O, Akin T, Najafi K. A wireless batch sealed absolute capacitive pressure sensor. *Sensors and Actuators A: Physical* 2001; **95**: 29–38.
- 27 Ong KG, Bitler JS, Grimes CA et al. Remote query resonant-circuit sensors for monitoring of bacteria growth: application to food quality control. *Sensors* 2002; **2**: 219–232.
- 28 DeHennis AD, Wise KD. A wireless microsystem for the remote sensing of pressure, temperature, and relative humidity. *Journal of Microelectromechanical Systems* 2005; **14**: 12–22.
- 29 Ong JB, You Z, Mills-Beale J et al. A wireless, passive embedded sensor for real-time monitoring of water content in civil engineering materials. *IEEE Sensors Journal* 2008; **8**: 2053–2058.
- 30 Wu S-Y, Hsu W. Design and characterization of LC strain sensors with novel inductor for sensitivity enhancement. *Smart Materials and Structures* 2013; **22**: 105015.
- 31 Kuo J-C, Kuo P-H, Lai Y-T et al. A passive inertial switch using MWNT-hydrogel composite with wireless interrogation capability. *Journal of Microelectromechanical Systems* 2013; **22**: 646–654.
- 32 Wu S-Y, Hung CY, Hsu W. A wirelessly readable and resettable shock recorder through the integration of LC circuits and MEMS devices. *Smart Materials and Structures* 2014; **23**: 095030.
- 33 Wu S-Y, Yang C, Hsu W et al. RF wireless LC tank sensors fabricated by 3D additive manufacturing. The 18th International Conference on Solid-State Sensors, Actuators and Microsystems (Transducers 2015); 21–25 June 2015; Anchorage, AK, USA; 2015: 2208–2211.
- 34 Eissa AA. Structure and Function of Food Engineering. InTech, West Palm Beach, FL, USA, 2012.
- 35 Nobel PA. Hypothetical model for monitoring microbial growth capacitance measurements – a minireview. *Journal of Microbiological Methods* 1999; **37**: 45–49.
- 36 U.S. Food and Drug Administration, Grade "A" Pasteurized Milk Ordinance, 2011 Revision, 2011; <http://www.fda.gov/downloads/Food/GuidanceRegulation/UCM291757.pdf>.



This license allows readers to copy, distribute and transmit the Contribution as long as it is attributed back to the author. Readers are permitted to alter, transform or build upon the Contribution, and to use the article for commercial purposes. Please read the full license for further details at <http://creativecommons.org/licenses/by/4.0>

Supplementary information for this article can be found on the *Microsystems & Nanoengineering* website (<http://www.nature.com/micronano>).